

Modelling local-phase of images and textures with applications in phase denoising and phase retrieval

Ido Zachevsky and Yehoshua Y. Zeevi

Abstract—The Fourier magnitude has been studied extensively, but less effort has been devoted to the Fourier phase, despite its well-established importance in image representation. Global phase was shown to be more important for image representation than the magnitude, whereas local phase, exhibited in Gabor filters, has been used for analysis purposes in detecting image contours and edges. Neither global nor local phase has been modelled in closed form, suitable for Bayesian estimation. In this work, we analyze the local phase of textured images and propose a local (Markovian) model for local phase coefficients. This model is Gaussian-mixture-based, learned from the graph representation of images, based on their complex wavelet decomposition. We demonstrate the applicability of the model in restoration of images with noisy local phase and in image retrieval, where we show superior performance to the well-known hybrid input-output (HIO) method. We also provide a framework for application of the model in a general setup of image processing.

I. INTRODUCTION

Inspecting images in the Fourier domain, one observes, as expected, that the magnitude and phase (A and ϕ , respectively) uniquely define an image. Inasmuch as there exists a one-to-one correspondence from A to the empirical autocorrelation, it follows that higher moments, and specifically edge-type image skeleton structures, are necessarily defined via the image phase, ϕ .

In natural stochastic textures (NST), an important facet of images that describes natural structure [1], [2], we recognize a subset of cases which is approximately Gaussian [2], and is therefore defined via its autocorrelation (second-order statistics). In this subset, the phase is random. On the other hand, natural images contain objects, separated from their background by edges and contours, that are dependent on their phase coherence for edge representation. Some NST do share this property in that their *global* properties may be Gaussian, as expressed via first and second order histograms, but they nevertheless have local structures that are not suitable for a Gaussian or any second order model.

It is, therefore, desirable to find a model or description for the *local phase* of such natural “structured stochastic” textures. The latter are defined as stochastic textures that incorporate phase structure. In such cases, applying noise or randomizing the phase will severely affect the appearance of the image. For example, we observe (Fig. 1) that the “cameraman” image (Fig. 1a) is non-Gaussian (indicated by high kurtosis) and severely affected by phase distortions, whereas the stochastic image (Fig. 1g) is closer to a Gaussian and is much less affected by the same phase distortion. The intermediate image (Fig. 1d) also shows dependency on its phase, although it

obeys Gaussianity, indicating that these type of images may benefit from a phase model.

The main contribution of this work is in providing a model for local phase coefficients; we review the importance of local phase, propose a model and method for estimating its parameters, and elucidate the usefulness of the proposed model by means of examples. An additional contribution is our novel phase retrieval algorithm, based upon our local phase model and the well-known HIO algorithm [3]. Since the proposed model can be used in Bayesian techniques, this is but one example of many other possible applications that can benefit from the proposed model.

A. The local phase

While a model for global phase is useful to some extent, in this work we are concerned with the characteristics of local phase, defined as the phase of a local structures. The local phase has several definitions, and it is either based on a windowed Fourier transform or on the phase coefficients of complex wavelet transforms or Gabor filters [4], [5]. There are advantages in analyzing local phase, as we know that image reconstruction via local phase yields better results compared with global phase-based reconstruction [6], and, in fact, the local phase portrays the basic image structure already in the first iterations of the reconstruction [4], [5]. Further, local analysis is computationally preferred in many cases, due to the simpler structures exhibited locally, compared with the complexity of modelling entire images as a whole.

The local phase has been successfully applied in edge detection in a method known as the phase congruency [7], which is an edge detection method that incorporates the phase, normalized by magnitude, thereby providing a detector which is invariant to various degradations and illumination changes in the image. So have been the zero crossings which are directly related to the local phase [8].

The main property inherited by the phase is the local coherence of different spatial frequencies, when they are in-phase (phase-locked). This can be seen by the definition of the Fourier transform, as well as by enforcing a constant magnitude to an image, observing that edges are retained. This is due to the fact that image are known to have a lowpass-type magnitude response, and enforcing a constant magnitude serves as a highpass filter that emphasizes edges and contours.

The coherence property is crucial in images since the magnitude energy is not enough for image comprehension; edges and skeletons are of utmost importance for image understanding and are defined by their coherence; a known example is the

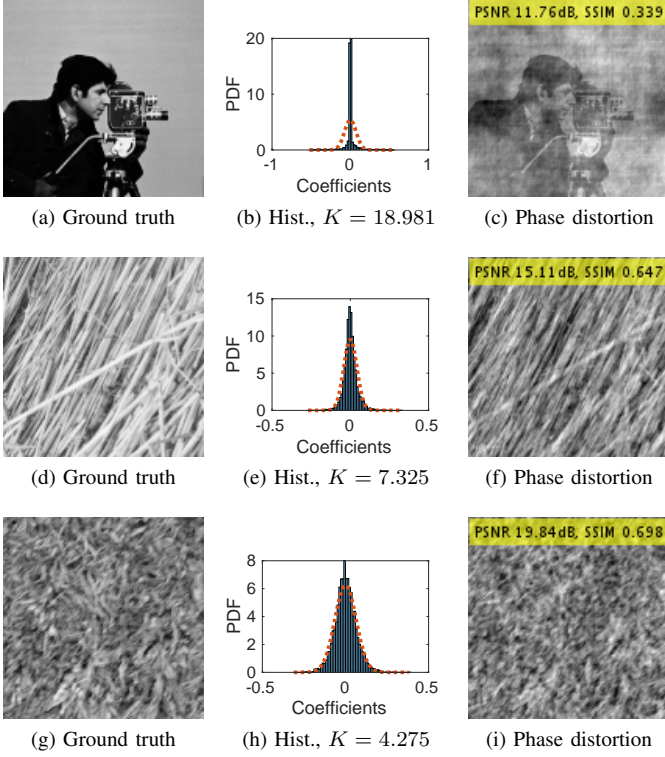


Figure 1: Gaussianity and phase distortion: Images with Gaussian behavior are less affected by phase deviation, indicating that they are less dependent on their phase. (a), (d) and (g): Ground truth images. (b), (e) and (h): Marginal histograms of wavelet coefficients with Gaussian fit (dashed red) and kurtosis value denoted by "K". (c), (f) and (i): Result of phase distortion by AWGN with $\sigma = 1$, for each of the ground truth images, respectively. PSNR and SSIM values indicated on the distorted image.

simple step, which requires that all the frequencies will be phase locked, i.e. have the same phase at the point of inflection and jump in intensity.

B. Modelling local phase

In modelling phase we observe that unlike magnitudes (i.e. the spectrum) that have a distinct exponential decay distribution, the phase distribution appears at first to be inherently noisy or random, and is assumed in many cases to be uniformly distributed. Consider a 2D magnitude with several distinct high-energy coefficients that define the main orientation of the patch. Other, less visible components, have lower energy.

The definition of the phase (as $\phi = \arctan 2\left(\Im \hat{I}, \Re \hat{I}\right)$ for \hat{I} , the Fourier transform of an image I) reveals that low energy coefficients, that have low energy values, will vary significantly in the range $[-\pi, \pi]$. Unlike the magnitude, in which insignificant coefficients have values close to zero, their phases will be approximately uniformly distributed. The incorporation of these ill-defined coefficients will have counterproductive

effect on any model we seek. They therefore have to be scaled according to their energy content.

Let us analyze an arbitrary patch, selecting only Fourier coefficients with high magnitudes. If this patch depicts some coherent structure (e.g. an edge), its selected set of high-magnitude coefficients will exhibit structure in their phase. Locally, we assume that structures are simple enough and therefore can be described by steps, ramps or points. Consider for example a patch that contains some oriented and uncentered edge. In the Fourier domain, this edge is described by some rotation and translation transformation of a centered and unoriented edge.

These transform rules reveal the instability of the phase and consequent challenge in its modelling; while a zero-mean, centered edge will be characterized by zero phase, a spatial shift by one pixel will yield linear phase with slope corresponding to the spatial translation distance.

In a densely scanned grid of patches, however, the same edge or otherwise coherent structure will at one point appear at the center of a patch. In the case of such a patch, the model is much simpler. Further, as edges tend to exhibit locally only a single orientation, anisotropic analysis is beneficial. Such an analysis is available in the form of Gabor filters or complex wavelets, that generalize the Fourier transform by incorporating scales and orientations in the image.

One method that captures such coherence is the phase congruency [9]. The phase congruency is, however, method of analysis. It has been used for edge detection [9], segmentation, fusion [10] and other tasks. Further analysis methods have been proposed for local phase, by proposing simple rules to link different coefficients, or parametric distributions for marginal histograms of phases [11], [12], [13], [14], [15]. These methods were used as well as indicators for segment detection, blur assessment and other tasks.

We, however, are interested in a complete model for the phase, that can in turn be used in a Bayesian framework. In the sequel, we present a graph- and wavelet-based image representation method and derive a Markovian (based on a local neighborhood) phase model for textures and images. This model is based on a mixture of Gaussians (GMM), which describes the local phase coefficient, given its neighborhood in the graph, by combining both spatial and scale relationships.

C. Wavelets for phase processing

Modelling both magnitude and phase can be accomplished by means of wavelet analysis. While we are interested in phase models, we should use a wavelet family, suitable for efficient processing in Bayesian frameworks with magnitude models as well. Such a framework should possess several properties: efficient inverse and forward transforms, orientational specificity and access to phase of local coefficients. These requirements are translated to using an orthogonal and discrete transform, an oversampled transform, and a complex transform, respectively.

We note that in the case of analysis (e.g. phase congruency), the Gabor basis or the Morlet wavelets in their continuous versions are used, as no inversion is required. A discrete, dyadic transform emerges due to the requirement of a discrete

and efficient transform. Dyadic transforms are more limited in their ability to exhibit phase responses, due to the sampling (decimation) of the coarser levels in each iteration. Nevertheless, we show in the sequel how they can be used for phase analysis.

A common property of discrete wavelet transforms is separability. This property renders wavelets to be much easier to apply and invert, but prevents orientational support. A wavelet family that satisfies all aforementioned requirements is the dual-tree complex wavelet transform (DTCWT) [6]. It is a twice-oversampled, complex coefficient, anisotropic wavelet transform. The DTCWT will be used in this work to model local phase.

D. Related works

Before presenting the graph-based model, we survey other phase-related studies. Local coherence has been investigated in [15], where the authors analyze the phase of symmetric linear-phase complex wavelets and show that given the self-similarity property in the Fourier domain:

$$F(f/s) = K(s) F(f),$$

where s is the scale parameter and $F(t)$ is the coherent feature in the transform domain, the phase of $F(t)$ in high scales is equal to the phase of lower scales. The authors show that this type of phase prediction and redundancy can be used for detecting blur in images. Blur, while not disruptive to global phase (for a large family of symmetric, zero-phase blur filters), does distort the local phase correspondence, as expressed by analyzing the local phase in different scales.

Direct application of the conclusions in [15] requires the application of a specific wavelet family; the authors used the complex steerable wavelets with linear phase, i.e. the wavelet function is a rotation of a prototype function, $f_s(t) = g(t) \cdot e^{-j\omega_c s}$, where $g(t)$ is the prototype symmetric low-pass filter with cut-off frequency ω_s . The linear phase property is required for this analysis.

In [16], an analysis of the phase was performed for three wavelet families, the DTCWT as well as the pyramidal dual-tree directional filter bank (PDTDFB) and the uniform discrete curvelet transform (UDCT). Here, the authors analyze the relative phase and propose statistical models for it. The authors fit different distributions for the marginal and joint histograms and use the distribution's parameters in characterising different textures.

The phase in the case of DTCWT, of interest in the context of our work, was analyzed in [12] by means of the so-called inter-coefficient product (ICP), which analyzes phases of adjacent scales. The ICP is a transform based on coefficient phase difference that achieves translation invariance in detecting orientational features in images. While it is an invertible transform, it is non-orthogonal. Thus, small changes in coefficients may propagate in an undesirable manner to the image space.

In [14], [13], the authors model phase relationship of adjacent complex wavelet scales to perform denoising. They enforce a certain property of the phase to yield more visually

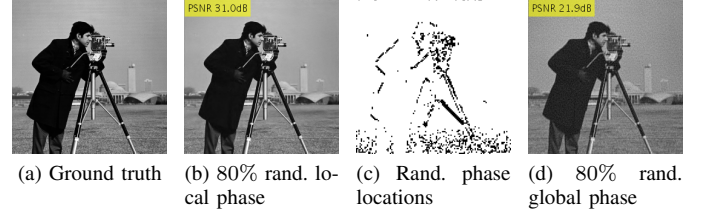


Figure 2: Effect of phase randomization: Randomizing 80% of DTCWT lowest-energy phase coefficients does not visually affect the image (b), unlike randomization of global phase (d). The randomized local coefficients belong to non-structured segments (c).

pleasing structures. It is worth noting that many applications of the phase (e.g. [17], [10]) have to do with using the edge map from phase congruency for segmentation, registration or other tasks that need the skeleton structure.

We also note the use of quaternion-based methods, that extend beyond complex numbers and provide further meanings to phases and magnitudes [18]. These methods are, however, beyond the scope of this paper.

II. WAVELET DECOMPOSITION AS A GRAPH

When modelling phase, it is important to separate the wheat from the chaff, since low-energy coefficients that do not reflect structure will affect estimated statistical models. We observe that keeping only high-energy phase coefficients, while randomizing low-energy ones, in the DTCWT domain, has negligible effect on the visual appearance of images. We, therefore, assume that the low-energy phase is less important.

In Fig. 2, for instance, we observe that randomizing 80% of the low-energy local phase components (in the DTCWT sense) has negligible effect on the image. Further, analyzing the randomized local phase coefficients, we observe that, as expected, most of the phase coefficients are discarded at non-edge points. On the other hand, keeping the same percentage of coefficients (20%) for the global phase, results in much different behaviour with visible artefacts (Fig. 2).

We represent an image by a graph as follows (Fig. 3, where the neighbors of a single coefficient, $c_{x,y}^i$, are depicted for a decomposition at level i with spatial location (x, y)): each wavelet coefficient entry has at most 9 neighbors: 4 spatial neighbors (in a 4-neighborhood system), 4 children that belong to the finer decomposition level and 1 parent that belongs to the coarser level.

In DTCWT, each decomposition level encodes information in 6 spatial orientations that provide, in turn, more details and orientational information than a standard discrete wavelet transform. The choice of 6 orientations rather than any other, arbitrary, number originated in vision research and was previously adopted in various schemes of image processing and computer vision [19].

Each node in the graph contains the magnitude and phase of all 6 orientations. Nodes on the graph's boundary that contain less than 9 neighbors are discarded in our analysis.

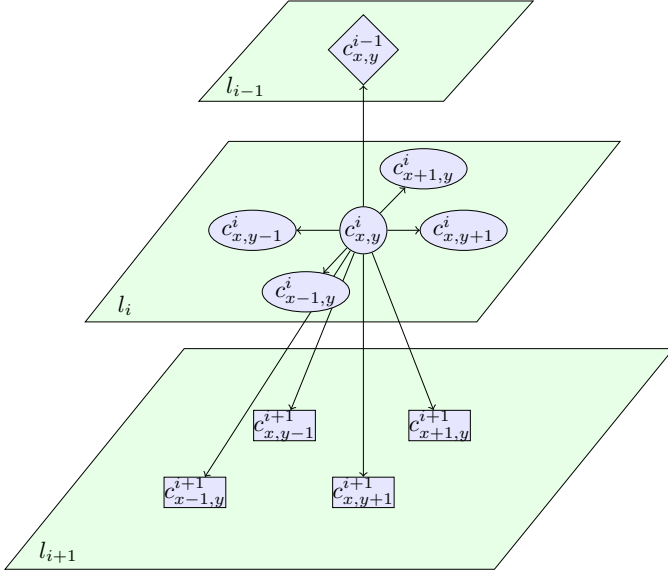


Figure 3: Local graph representation of a wavelet coefficient $c_{x,y}^i$ on level i and at spatial location (x,y) . Ellipses represent spatial translations, rectangles represent finer levels and the diamond represents the coarser level. l_i denotes the i th decomposition level.

The exact neighborhood structure is derived from the wavelet transform used in the graph decomposition. The proposed graph structure depicted in Fig. 3 has 4 children per node, that provide finer details in 4 projections of the same spatial location. Other wavelet transforms may yield different graph decomposition structures, but the same principal will be retained. We use the term “neighbors” as it is commonly used to denote neighbors in a graph, but we note that while neighbors at the same level (e.g. Fig. 3, level l_i) belong to adjacent spatial locations, neighbors in adjacent levels (e.g. l_{i-1}, l_{i+1}) have the same spatial location, but different wavelet frequency bands.

As an example of possible use of the graph, let us consider paths of coarse-to-fine coefficients (i.e. a vector in the size of the transform depth). Each such path starts from the finest coefficient and finishes at the coarsest level, and for each finest coefficient we have 6 originating paths, one for each orientation. In this case, we consider a *low-energy path*; i.e. a path with average coefficient magnitude lower than a certain threshold.

Before resorting to complete modelling, we would like to gain first some intuition on the graph structure. It is interesting to note that randomization of phases in low-energy paths yields smoothing of fine details, while retaining large-scale features (Fig. 4).

Analyzing the phase for high- and low-energy paths reveals a different distribution for each case. We observe that in the high magnitude paths, the marginal cdf of phase coefficients is not uniform, unlike the low-magnitude paths (Fig. 5). This was evaluated on the “cameraman” image. The same behavior was observed in other images.

A similar phenomenon is observed by inspecting 2D his-



(a) Ground truth (b) 29% rnd. pha. (c) 76% rnd. pha. (d) 97% rnd. pha.

Figure 4: Phase randomization of DTCWT paths: Images with randomized phase paths are shown with ascending extent of randomized content. Images in (b), (c) and (d) depict results of phase randomization of 29%, 76% and 97% of the coefficients, respectively. The images with randomized phase appear natural due to randomness of complete paths.

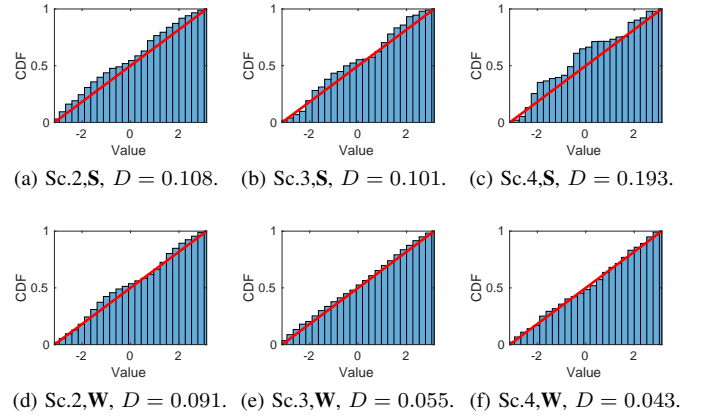


Figure 5: Cdf of marginal histograms of wavelet coefficients of the first orientation of the “cameraman” image. Phase coefficients corresponding to high magnitudes (strong, denoted “S”) deviate from the uniform distribution, whereas phase coefficients corresponding to low magnitudes (weak, denoted “W”) are of a distribution closer to uniform. Figs. (a), (b) and (c): Strong coefficients of scales 2, 3 and 4 (denoted by “Sc.”), respectively. Figs. (d), (e) and (f): Weak coefficients of scales 2, 3 and 4 (denoted by “Sc.”), respectively. The maximal difference between the cdf of the empirical and the uniform distribution are denoted by “D” on each figure.

tograms, revealing dependency. We calculate the joint empirical pdf of the *phase difference* between the second-third and third-fourth scales (Fig. 6), and compare the maximal count frequency (most occurring combination) between high- and low-energy coefficients, defined by thresholding the magnitudes.

To observe this phenomenon better, we analyze the coefficients over a range of thresholds, for 20% to 7% of the strongest coefficients (this range captures the differences between the high- and low-energy coefficients), and observe that the maximal count frequency for high-energy coefficients is considerably higher in almost all cases, indicating that this phenomenon does not depend considerably on the threshold (Fig. 7).

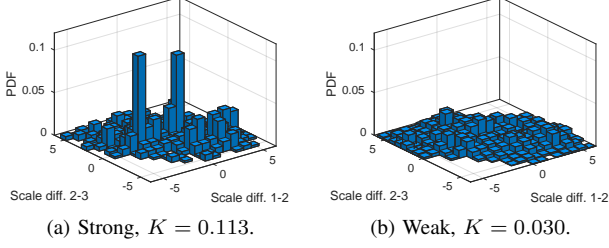


Figure 6: Pdf of adjacent scale joint histogram of wavelet phase coefficient difference of the "cameraman" image. Phase coefficients corresponding to high magnitudes ("Strong") are distributed differently than coefficients corresponding to low magnitudes ("Weak"). Figs. (a) and (b): Strong and weak joint histograms of phase coefficient differences, respectively. The kurtosis of each empirical distribution are denoted by "K" on each figure.

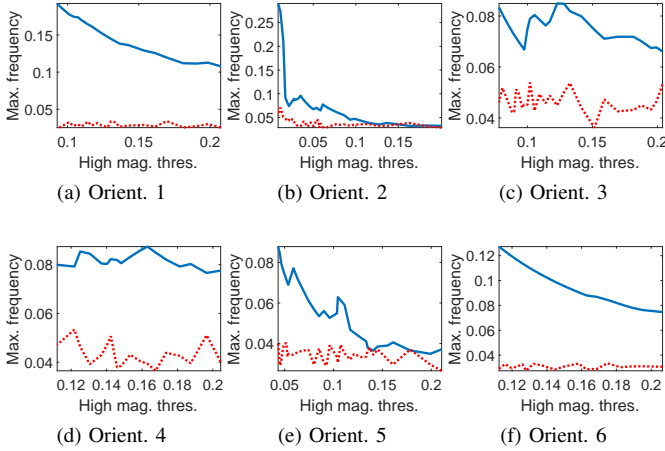


Figure 7: Maximal count frequency for phase difference joint histograms. Phase coefficients corresponding to high magnitudes have much higher maximal frequencies (denoted by solid blue lines), revealing less random behavior, compared with low-energy coefficients (denotes by dashed red lines). (a)–(f) show maximal frequencies of orientations 1–6, respectively (denoted "Orient."), for varying thresholds of high vs. low magnitudes.

The high maximal frequency in the examples (Fig. 7 and Fig. 6) corresponds to a peak in the probability distribution of the coefficients. This indicates that for high-energy coefficients, there is lower variance in the probable values than for low-energy coefficients, corresponding to image structure encoded in the former.

III. A GAUSSIAN MIXTURE MODEL FOR LOCAL PHASE

Due to statistical dependencies between adjacent scales and spatial locations, observed in this work and elsewhere, we model a phase coefficient along with its immediate neighborhood, as expressed in the local graph excerpt (Fig. 3). We thereby have an underlying Markov assumption, that phase

coefficients can be described by means of their local neighbors. This modelling allows us to estimate distributions based on moderately-sized image banks, due to the fact that the dimension of the random vector is 10 (Section II). Following our discussion as to the importance of thresholding high-energy coefficients, our model is based on high-energy coefficients only, where the threshold is a parameter that needs to be imposed. In our experiments we set the threshold so that 20% of highest magnitudes are considered.

We define the sub-tree as an excerpt of the complete wavelet graph tree (Fig. 3); it is vectorized to a 10-dimensional vector, v , as follows: $v(1)$ is the middle node, $v(2), \dots, v(5)$ are the adjacent nodes in the same level, $v(6), \dots, v(9)$ are the child nodes, and $v(10)$ is the parent node. Using the notations of Fig. 3, we have

$$v = [c_{x,y}^i, c_{x-1,y}^i, c_{x,y-1}^i, c_{x+1,y}^i, c_{x,y+1}^i, c_{x-1,y}^{i+1}, c_{x,y-1}^{i+1}, c_{x+1,y}^{i+1}, c_{x,y+1}^{i+1}, c_{x,y}^{i-1}]. \quad (1)$$

The sub-trees considered for learning are only "full" neighbors that belong to the detail wavelet coefficient. We do not model the approximation (scaling) decomposition level. We use 384 images, randomly selected from the Brodatz and McGill texture datasets, cropped to size $N \times N$, where $N = 256$ with 4 wavelet decomposition levels. From each image we extract the $N^2/64$ coefficients with the highest magnitudes and their respective sub-trees, which yields the approximate 20% threshold.

We train the GMM via the expectation-maximization (EM) algorithm. The number of parameters to be learned is defined as:

$$n_{params} = (m^r + m) \cdot k + k,$$

where m is the vector's dimension, k is the number of components, and the value of r is either 1 or 2, depending on the covariance structure, where $r = 1$ for diagonal covariance and $r = 2$ for full covariance. In our case, $m = 10$, $k = 10$ and $r = 1$. The reasoning for selecting $k = 10$ is explained in the sequel. We define the following ratio:

$$r_{params} = n_{samples} / n_{params},$$

where $n_{samples}$ is the number of samples available for learning. To provide sufficient samples for EM-based learning, we demand $r_{params} > 50$, so that for each parameter learned there are at least 50 samples.

Despite the fact that we observe dependencies in joint histograms of phase differences (e.g. Fig. 6), we learn the phases values without applying any difference or other linear schemes, under the assumption that the EM algorithm will learn the underlying structure of the phase, provided there are sufficient samples.

In the sequel we demonstrate the properties of the learned phase model as well as use it for various applications in image processing.

A. Choosing the right number of components

Gaussian mixtures can effectively describe any distribution, provided the number of components is high enough. However,

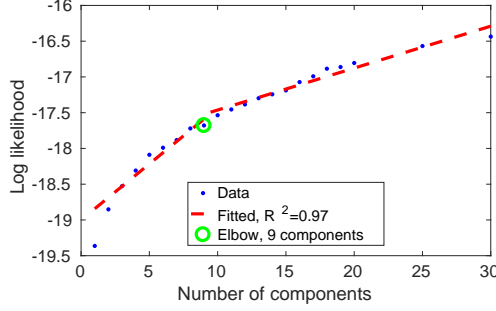


Figure 8: Estimating the number of components for modelling local-phase with GMM. The elbow was found to be between 5 and 10 components.

using too many Gaussian components can lead to over-fitting and loss of generality. We use K-fold cross validation to choose an optimal number of components. Given a set of M sub-tree vectors, we partition the dataset to $U = 10$ randomly selected equal subsets. We then train the GMM for K components using all but one subset, and calculate the mean of the log-likelihood of each of the left-out variables. This is iterated U times, where at every iteration, a different subset is left out. The mean log-likelihood is then averaged again across all iterations. The result provides a scalar number that indicates how good is the definition of the test data (the left-out subset) according to the model trained by the data.

The optimal mixture number is selected by finding the so-called *elbow* in the mean log-likelihood, plotted against the number of components. More components will describe the test data better, due to more dense filling of the feature space and will therefore not decrease, but the contribution of more components after a certain threshold will be marginal. This is indicated by an elbow in the mean log-likelihood vs. number of component, and this is the chosen number of mixture components we use [20, §14]. We observe that a number of 5 to 10 components, as used in this work, fits the elbow assumption (Fig. 8). The elbow was found automatically by fitting two first order polynomials to the log-likelihood of the test set, when the GMM has been fitted based on the training data with a set number of components. We note that the use of 10 components instead of 9 (Fig. 8) does not affect the model in any noticeable manner.

Since in all our experiments (including those that are not shown here) we use up to 30 components, a large amount of data is required for training. The aforementioned number of images (384) yields a ratio of samples to trainable parameters of at least 600 and the number of sub-tree vectors used was $M \approx 393 \times 10^3$, verifying that sufficient data was available.

B. Demonstration of the phase model

The learned model yields $K = 10$ normally distributed components. In this section, we demonstrate intimate relationship between the learned coefficients and the visual aspects that relate to coherent structures. We define the average congruency

(AG), similarly to the phase congruency [9], as follows:

$$AG(k) = \left| \frac{1}{M} \sum_{m=1}^M \cos(\eta_k(m) - \bar{\eta}_k) \right|,$$

where M is the number of scales considered in the model (in our case $M = 3$ since we analyze a tree that spans at most three scales), where lower values of m correspond to coarser scales; k is the component number, $\eta_k(m)$ is the mean value of the phase at the m th scale in the k th component, as learned via the Gaussian model. $\bar{\eta}_k$ is the mean value of η_k . Using the sub-tree structure (1) we define:

$$\begin{aligned} \eta_k(1) &= 2^1 \cdot \mu_k(10) \\ \eta_k(2) &= 2^0 \cdot \mu_k(1) \\ \eta_k(3) &= 2^{-1} \cdot \left[\frac{1}{4} \sum_{i=6}^9 \mu_k(i) \right]. \end{aligned}$$

This is explained as follows: the first mean phase coefficient is the coarser phase, $\mu_k(10)$. The next phase coefficient is the central phase coefficient, $\mu_k(1)$, and the finest phase coefficient is a mean of the four children phase nodes, $\mu_k(i)$ for $i = 6, \dots, 9$. The phases are normalized by powers of 2 according to their relative scales to compensate for the dyadic decimation that affects the phase, as was described elsewhere [14], [13].

The average congruency, $AG(k)$, reflects the phase congruency quantity [7] for cases in which the magnitude is equal in all coefficients. The value of $AG(k)$ reflects the same meaning as the original phase congruency, as low values (close to 0) correspond to incoherent structures with phases in random directions, whereas high values (close to 1) correspond to coherent structures in which all the cosines are close to 1.

We use this quantity to assess the coherence of each component in the Gaussian mixture; we expect the model to learn components that correspond to high $AG(k)$ values and represent coherent structures, as well as components that correspond to low $AG(k)$ values and represent incoherent structures.

To demonstrate this effect, we train the model using 20 images from the Brodatz dataset. We then decompose an image with coherent structures to its wavelet graph (Fig. 9), and for each pixel in the intermediate scales we calculate the posterior component, $\mathbb{P}\{k|y\}$. Given a component number, k , we place markers on the decomposition images if the coefficient was derived from the k th component, defined as the component that maximizes the posterior probability, provided the probability is higher than a threshold set to 0.8.

Using this demonstration scheme, we plot the markers on the decomposition images for several values of k , which correspond to components with different values of $AG(k)$. We observe that, indeed, when we choose k with high $AG(k)$, the markers are placed on edge-type structures, and vice versa; low values of $AG(k)$ correspond to coefficients that contain mostly noise or other non-coherent structure.

Further, we expect the model to capture various degrees of coherence, varying from very coherent to non-coherent coefficients, as observed in the learned model (Fig. 10).

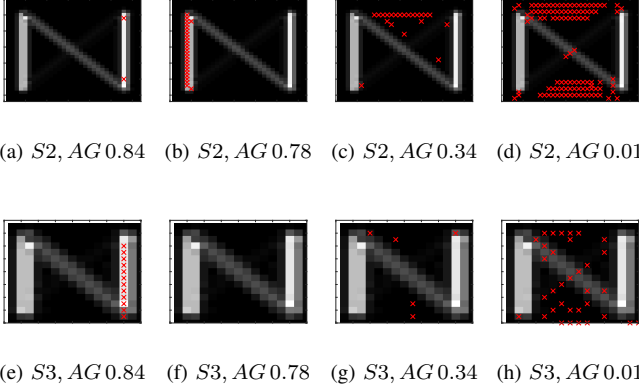


Figure 9: Demonstration of the local phase model using a synthetic image. Shown is the third orientation. First and second rows depict the second and third wavelet scales, respectively. The columns correspond to components in decreasing values of average congruency; in the first two columns we depict the two highest values and in the last columns depicted are the lowest two values. The red markers highlight coefficients that maximize the posterior for the given component. We observe that components with high values of average congruency are the posterior components for coherent local structures, such as edges, whereas less order and coherence is observed for structures with posterior components of low average congruency.

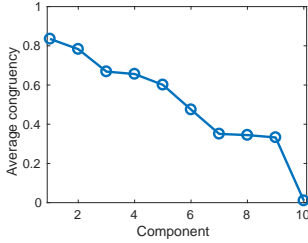


Figure 10: The average congruency as captured by each component of the model (in descending order). The model captures various degrees of congruency.

IV. PHASE ESTIMATION UNDER NOISY CONDITIONS

The first application we present is useful when the local phase is noisy, due to distortions or lossy coding of the coefficients. We use this scheme in order to demonstrate the efficacy of the proposed model; we therefore show several examples of noisy phase which distorts the image structure, and the reconstructed versions using the proposed model.

Let $\eta \sim \mathcal{G}$ denote the detail phase coefficients and the learned GMM distribution, \mathcal{G} . Let θ denote the noisy phase:

$$\theta = \eta + w,$$

where w is white Gaussian noise with variance σ^2 . We

estimate η given θ :

$$\begin{aligned} \hat{\eta}(\theta) &= \mathbb{E}\{\eta|\theta\} = \int x p_{\eta|\theta} dx \\ &= \int x \frac{p_{\theta|\eta} p_{\eta}}{p_{\theta}} dx = \frac{1}{p_{\theta}} \int x p_{\theta|\eta} p_{\eta} dx. \end{aligned}$$

The distribution of the noisy coefficients, p_{θ} , is also a GMM [21] with the same parameters other than the covariance which satisfies $\Sigma'_k = \Sigma_k + \sigma^2 I$, where Σ'_k and Σ_k are the k 'th covariances for θ and η , respectively. This also provides means to estimate the GMM component covariances given the noisy patch.

p_{η} is the probability for the learned GMM. $p_{\theta|\eta}$ is the noise distribution with parameter $\theta - \eta$:

$$q(\theta - \eta) \triangleq p_{\theta|\eta}(\theta, \eta) = \mathcal{N}(\theta - \eta; 0, \sigma^2 I).$$

The joint distribution is

$$p_{\theta|\eta} p_{\eta} = \sum \pi_k g_{\eta}^k \cdot q(\theta - \eta),$$

and the final estimation is given by [21]:

$$\hat{\eta}(\theta) = \frac{1}{p_{\theta}} \sum_{k=1}^K \pi_k g_{\theta}^k \cdot (\Sigma'_k)^{-1} (\sigma^2 \mu_k + \Sigma_k \theta). \quad (2)$$

We note that this can be extended to manifold-type processing or EPLL-type processing to yield better results than scalar-wise estimation. The EPLL and manifold equations should be similar to the usual methods [22], [23] with the distinction that they are applied on a tree structure.

A. Experiments

We apply AWGN on the detail phase coefficients of images in the DTCWT domain (the approximation level is not affected). Applying noise on the phase distorts local structures severely, and edges and other structures appear smeared (Fig. 11). We then apply the denoising scheme (2) on all detail coefficients' phases.

In many cases, not all 9 neighbors are available, for example in the coefficients of the finest level. In these cases, we use the model coefficients that are present in the coefficient's neighborhood. We emphasize that the experiments were not performed on images used for learning. Further, the model was trained on texture datasets (Brodatz and McGill), but was still used to denoise natural images as well.

Inspecting the results (Fig. 11), we observe that fine detailed structures, degraded severely by the phase noise, were made more coherent, rendering the image to become more visually appealing. We observe also the significant improvement in the SSIM (superimposed on each figure), due to the improved structures in the reconstructed images. These results, of images of various modalities - both natural and textured images - demonstrate the efficacy of the phase model in its ability to reconstruct local structures.

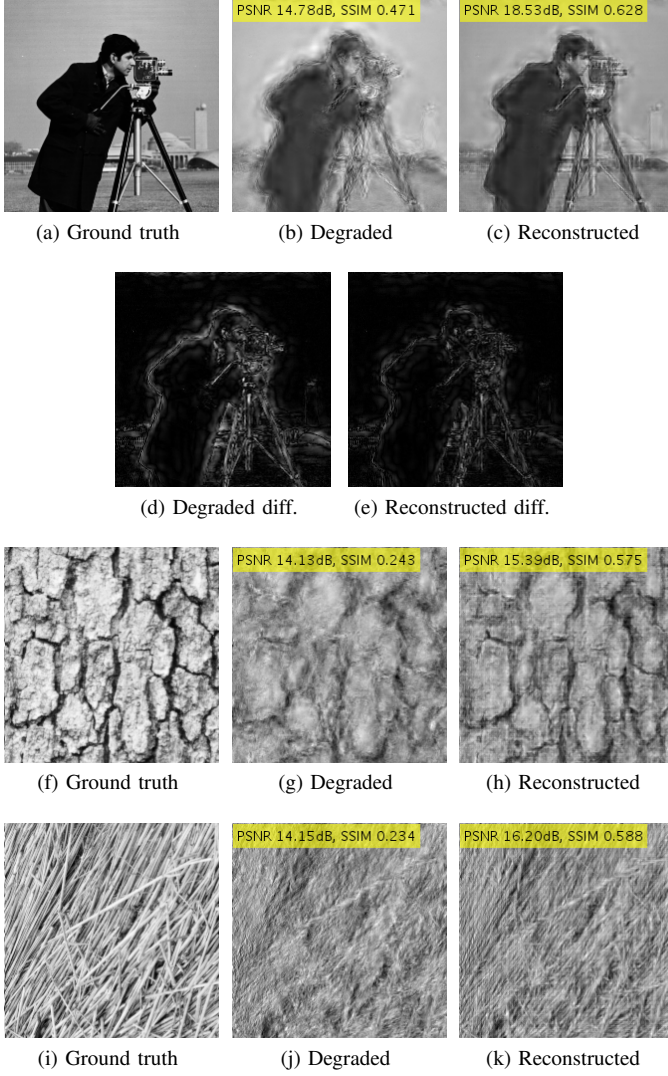


Figure 11: Phase denoising example. The image is degraded by noisy local phase ($\sigma = 2$) in its detail coefficients (b) depicts distorted local structure. The reconstructed image (c) has recovered structure, noticeably in the face and camera area. The absolute difference between the ground truth (a) and the degraded and reconstructed images, shown in (d) and (e), respectively, illustrate that the reconstructed image has recovered some missing structure. Two additional examples are provided in the third and fourth rows: (f), (g), (h): Ground truth, degraded and reconstructed images, respectively; (i), (j), (k): ground truth, degraded and reconstructed images, respectively. PSNR and SSIM values are superimposed on each image.

V. PHASE RETRIEVAL USING THE LOCAL PHASE MODEL

As a second application based on the local phase, we present a phase retrieval algorithm using the local phase model. It is a novel, unexpected, idea to show that local phase models can be used in global phase restoration, as is considered in the phase retrieval problem. This important property is demonstrated in Fig. 12 and further elaborated in Appendix

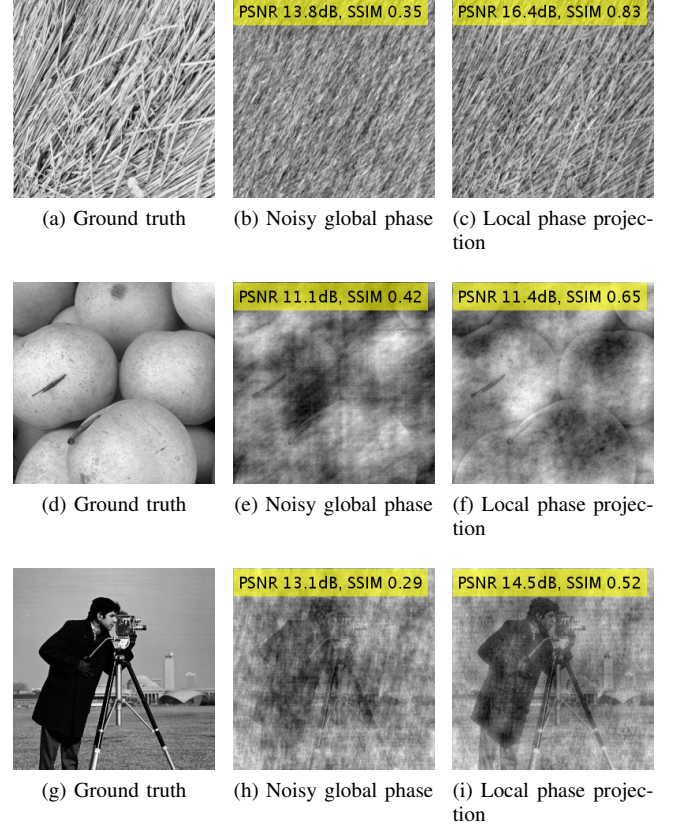


Figure 12: Local phase facilitates global phase reconstruction. Examples of natural texture, natural image and man-made are shown in the left column ((a), (d) and (g), respectively). Gaussian noise with $\sigma = 1.5$ is applied to the global phase of the ground truth images ((b), (e) and (h), respectively). Images with restored (projected) ground truth local phase are shown in (c), (f) and (i), respectively. PSNR and SSIM values are superimposed on each image. The images in the right column illustrate that the projection of the local phase improves the edge structure of the image with distorted global phase.

A. In the Figure, we observe that using the ground truth local phase obtained from the wavelet graph, restores fine-details of edge structure in images with global phase distortion. This apparent relationship between the local and global phase is the subject of this section, wherein we exploit the local phase model for the benefit of the phase retrieval problem, in which case the global phase is unknown.

Phase retrieval is the process of reconstructing an image in the space domain, $I(x, y)$, given only its Fourier magnitude, $|\hat{I}(u, v)|$. That is, the phase, $\angle \hat{I}(u, v)$ needs to be recovered and the image thereby reconstructed. This is commonly solved iteratively by imposing known constraints in the space domain, e.g. non-negativity and support, and then imposing complementary constraints in the frequency domain, usually the known magnitude. This process is iterated until the image is restored, or a given error criterion is achieved.

The error measure commonly used for phase retrieval is the

error in the frequency domain [24]:

$$\epsilon_t = |||\hat{I}| - |\hat{I}_t|||_2^2, \quad (3)$$

where \hat{I}_t is the Fourier transform of the restored image in the t th iteration. A well-known algorithm used for phase retrieval is Fienup's hybrid input-output (HIO) algorithm [3], [25], that will be used as a benchmark in our experiments.

Phase retrieval is still a challenging problem in imaging and image processing. There has been considerable advancement in solving the problem for 1D or sparse signals [25], [26], [27], or by using methods that require matrix lifting, which renders the algorithms to become inefficient even in the case of moderately sized 2D images [28].

When we turn to solving the phase retrieval problem for 2D, non-sparse, moderately-sized images, we observe that HIO remains a preferred choice [28]. It is based on alternating projections, which does not entail working in higher dimensions. Using the HIO algorithm as our benchmark serves two goals: first, it is a widely-used phase retrieval algorithm. Second, it allows us to introduce a simple method that improves it, which does not necessitate any new assumptions (such as sparsity or maximal signal dimension).

To introduce the local phase model in phase retrieval, we modify HIO by adding local phase denoising steps. We first model the local phase as noisy with variance $\sigma_n^2(i)$ where i is the iteration number, and apply the phase denoising scheme (2) every N_{est} iterations of the HIO algorithm. The complete local phase-based phase retrieval algorithm (denoted local phase HIO or LPHIO) is denoted by Alg. 1.

To train the phase model, we use, as described earlier, 384 $N \times N$ -sized images from Brodatz and McGill datasets (cropped) with $K = 10$ Gaussian mixture components. Estimation of the phase noise variance in each iteration is a subject of further discussion, as the wrapping of the phase discourages using usual noise estimation techniques; Euclidean distances (as measured by the variance) might not reflect the true noise in the coefficients. Instead, we use the following noise model: $\sigma_n^2(i) = a \cdot \exp\{-b \cdot i/T\}$, where a is the initial noise estimate, b determines the rate of decay and T is the number of iterations. We use the same values of a , b and T in all experiments.

The evaluation of the algorithm is performed as follows: images of size $N \times N = 128 \times 128$ that are padded to size $2N$ along each dimension are used. The $D = 15$ images are of different modalities (texture, structured texture man-made and natural images; Fig 13). We note that these are arbitrary images taken from MATLAB's image database. The algorithm is evaluated using the following parameters: $T = 1500$, $N_{est} = 50$, $a = 2$, $b = 5$. We measure the Fourier domain error (3), the PSNR and SSIM of the restored images. Since the restored images may be rotated by 180° due to the phase ambiguity, we measure the PSNR and SSIM w.r.t both the rotated and non-rotated images and consider the maximal value. For each image, we initialize the phase randomly $P_{init} = 5$ times, for assuring that the result is not due to different initializations of the phase. The total number of experiments is $N_{exp} = D \times P_{init} = 75$. Fig. 14 shows an example of several image results.

Algorithm 1 The local phase HIO (LPHIO) algorithm. The local phase estimation step 4 is evaluated every N_{est} iterations. The rest of the algorithm is identical to HIO.

LPHIO phase retrieval algorithm. Inputs: Fourier magnitude $|\hat{I}|$, space-domain support S , phase model Φ , number of iterations T , local phase estimation frequency N_{est} , expected noise per iteration, $\sigma_n^2(i)$, $i = 0, \dots, T$ and HIO scaling parameter β .

Denote by $\hat{\phi}^i$ the phase estimation in the i th iteration. Assume $\hat{\phi}^i$ is initialized as uniformly distributed random phase ($\mathcal{U}[-\pi, \pi]$).

For $i = 1, \dots, T$:

- 1) Estimate image using the known Fourier magnitude and phase estimate: $I^i(x, y) \leftarrow \text{Real} \left\{ \mathcal{F}^{-1} \left\{ |\hat{I}| e^{j\hat{\phi}^{i-1}} \right\} (x, y) \right\}$.
- 2) $V(x, y) \leftarrow \{x, y : \bar{S}(x, y) \vee \{I^i(x, y) < 0\}\}$
- 3) $\hat{I}^i(x, y) \leftarrow \begin{cases} I^i(x, y), & V(x, y) = 0 \\ I^{i-1}(x, y) - \beta \cdot I^i(x, y), & V(x, y) = 1 \end{cases}$
- 4) If $\text{mod}(i, N_{est}) = 0$, perform local phase estimation:
 - a) Extract the top-left $N \times N$ image $I_{tl}^i(x, y)$ from $\hat{I}^i(x, y)$.
 - b) Estimate local phase for $I_{tl}^i(x, y)$ given Φ and $\sigma_n^2(i)$ to yield $\hat{I}_{tl}^i(x, y)$ using (2).
 - c) Set the top-left $N \times N$ image of $\hat{I}^i(x, y)$ to $\hat{I}_{tl}^i(x, y)$.
- 5) $I^{i+1} \leftarrow \hat{I}^i$
- 6) $\hat{\phi}^{i+1} \leftarrow \angle \mathcal{F} \{I^i(x, y)\}$

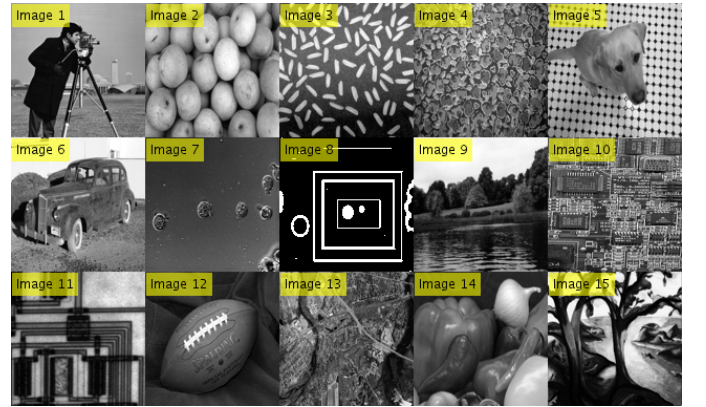


Figure 13: Image dataset used in evaluation of phase retrieval: the images used were natural, man made and structured texture.

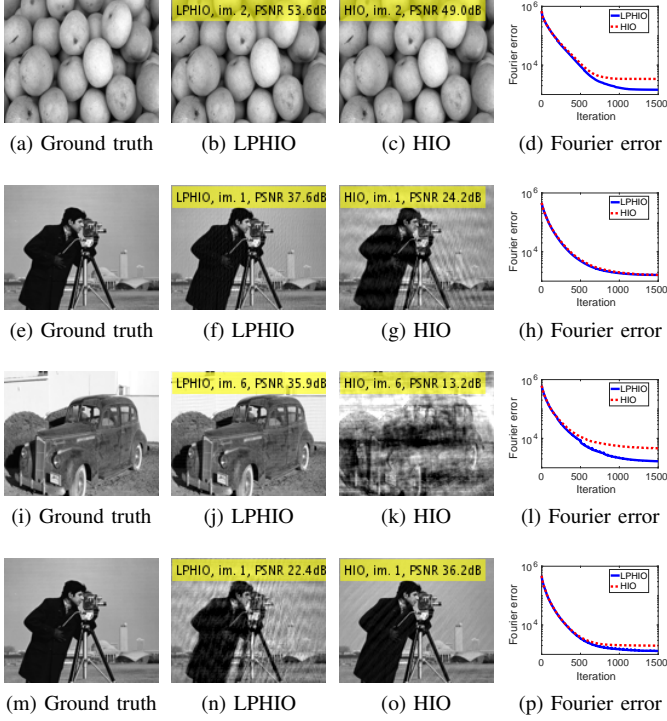


Figure 14: Characteristic examples of (cropped) images and phase initializations for phase retrieval using LPHIO. First column ((a), (e), (i) and (m)) depicts ground truth images, second column ((b), (f), (j) and (n), respectively) provides the results obtained by means of the proposed algorithm (LPHIO), on the third column ((c), (g), (k) and (o), respectively) are the HIO results and the fourth column ((d), (h), (l) and (p), respectively) shows the Fourier domain errors, where LPHIO and HIO are shown in solid blue and dashed red lines, respectively. PSNR figures are superimposed on the reconstructed images. We observe that the Fourier error decreases with iterations. Rows 1–3 show examples of better LPHIO performance and the fourth row shows better HIO performance in terms of PSNR (o) whereas the Fourier error (p) was better for LPHIO.

The N_{exp} experiments are analyzed together by evaluating both the Fourier domain error and the PSNR with respect to the ground truth. We note that Parseval’s theorem does not hold in this case, since we calculate the Fourier domain error for coefficients of the zero-padded image (to size $2N \times 2N$), whereas we calculate the PSNR only for the on-support image, of size $N \times N$.

Two measurements, the Fourier domain log-error difference (d_F) and the PSNR difference (d_P), are shown for each image, when using the proposed algorithm (LPHIO) vs. standard HIO (Fig. 15). These measurements are defined as:

$$d_F(k) \triangleq \log \epsilon_t^{LPHIO}(k) - \log \epsilon_t^{HIO}(k)$$

$$d_P(k) \triangleq \text{PSNR}\left(I_k, \hat{I}_k^{LPHIO}\right) - \text{PSNR}\left(I_k, \hat{I}_k^{HIO}\right),$$

where k is the image index, ϵ_t^A is the Fourier domain error for algorithm $A \in \{\text{LPHIO}, \text{HIO}\}$, I_k is the ground truth k th

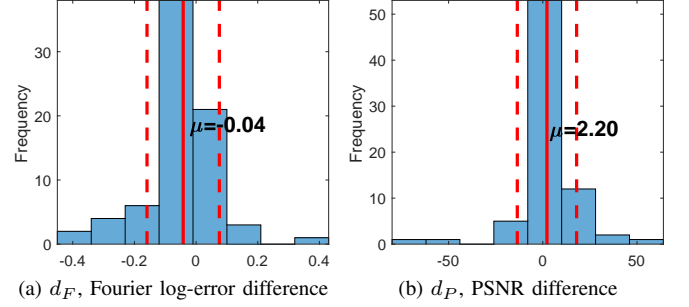


Figure 15: Comparison of LPHIO and HIO phase retrieval. Negative values indicate lower figures for LPHIO compared with HIO. The mean and standard deviation are highlighted by solid and dashed lines, respectively. The mean for the Fourier domain error distance (a) was negative and the mean for the PSNR difference (b) was positive, indicating that on average, the LPHIO yielded better results in both Fourier and object domains.

image and \hat{I}_k^A is the reconstructed k th image using algorithm A . Histograms for $d_F(k)$ and $d_P(k)$ show that on average, the LPHIO yields lower Fourier domain error and higher PSNR compared with HIO. LPHIO therefore yields better objective results in both metrics.

VI. IMAGE PROCESSING SCHEME INCORPORATING THE PHASE MODEL

As a final example, we provide a framework for image processing using the phase model. The phase is expressed by means of the complex wavelet coefficients as follows:

$$\angle x = \arctan 2(\Im x, \Re x),$$

where $\arctan 2$ is the function with suitable quadrant selection. It is observed that even in the case where a model of the phase is obtained, a direct application of the phase model to the space domain is not trivial.

Consider the following problem:

$$y = Hx + n,$$

where x , n and y are the ground truth, independent noise source and the degraded image, respectively. H is assumed to be a known linear operator, e.g. blur. Restoration is performed by solving the following MAP problem:

$$\hat{x} = \arg \max_x \mathbb{P}\{y|x\} \mathbb{P}\{x\}.$$

Let $w = Wx$ denote the wavelet coefficients of $x = W^{-1}w$ and W denote the wavelet transform. Then,

$$\begin{aligned} \hat{x} &= \arg \min_x (-\log \mathbb{P}\{y|w\} - \log \mathbb{P}\{w\}) \\ &= \arg \min_x \frac{1}{2\sigma_n^2} \|HW^{-1}w - y\|^2 + f(w) \\ &\triangleq \arg \min_x \beta \|HW^{-1}w - y\|^2 + f(w). \end{aligned}$$

Direct application of the phase model here is challenging, since w is complex and we model its phase. Instead, we

have access to $\mathbb{P}\{\angle w\}$. Denoting $a_w \triangleq \angle w$, we present the following formulation, known as half quadratic splitting [22]:

$$L = \beta \|HW^{-1}w - y\|^2 + \alpha \|a_w - z\|^2 - \log \mathbb{P}\{z\}. \quad (4)$$

Problem (4) yields the best match of w to both minimization of the likelihood term and maximization of the probability of the phase when $\alpha \rightarrow \infty$. The intermediate term, $\|a_w - z\|^2$, acts as a surrogate that links the phase prior with the signal fidelity. The standard method of solving this problem is by iterating with increasing values of α , where in each iteration, the minimization problem of L for w given z is solved first, and the second stage is the alternate minimization (z given w).

The first problem entails solving

$$\hat{a}_w = \arg \min L_1 := \beta \|HW^{-1}w - y\|^2 + \alpha \|a_w - z\|^2$$

for a_w , where $a_w = \angle w$. The intuitive meaning of this problem is to find the best coefficients for the fidelity term that have the local phase given by z . This problem is approximated by iterative projections:

$$\begin{aligned} \hat{w} &:= \hat{w} - \lambda \nabla_{\hat{w}} \left[\|HW^{-1}\hat{w} - y\|^2 \right] \\ \angle \hat{w} &:= z, \end{aligned}$$

until convergence.

The second problem requires solving

$$\hat{z} = \arg \min L_2 := \alpha \|a_w - z\|^2 - \log \mathbb{P}\{z\}.$$

This kind of problem is now detached from the meaning of the coefficients (phase) and was solved approximately elsewhere (e.g. [22]). The approximation entails calculating the posterior of the Gaussian components, $\hat{k} = \arg \max_k \mathbb{P}\{k|z\}$, and choosing the distribution as a single Gaussian of the \hat{k} 'th Gaussian in the mixture. Then, a MAP estimate can be formulated in close form:

$$\hat{z} = (\Sigma_{\hat{k}} + \alpha I)^{-1} (\Sigma_{\hat{k}} a_w + \alpha I \mu_{\hat{k}}).$$

VII. DISCUSSION AND FURTHER WORK

While the importance of phase has been investigated thoroughly in recent decades, much of the results were of projection algorithms to some constraints set or likelihood models. In this work we provided a prior model that can be used in Bayesian settings and illustrated several applications.

Using the prior model for phase retrieval has been demonstrated for arbitrary images that do not belong to the domain of the trained model (i.e. textures), thereby indicating the generality of the local phase model. It is our underlying assumption that images are characterized by the same overall behaviour as the learned images. This assumption renders our algorithm to be less restrictive than other phase retrieval algorithms that assume sparsity in the object domain [25], or some strict knowledge of the true global phase [24].

In a discrete wavelet representation of images, we decompose the image several times, so that the final approximation coefficients provide little information concerning fine image details. They encode background information of lower frequencies. In this study, we did not model these coefficients,

since their phase is less pronounced. However, it is interesting to provide a joint model of details and approximation coefficients, and to compare it with the proposed model.

Decomposing an image by means of wavelets is a well-known method of image analysis. However, the application of this technique as presented in this work, by locally modelling space and scale coefficients, was not considered in this form earlier. In other studies, image phase is considered to be a global property, or a property that is related only to scale. The proposed graph representation encapsulates both spatial and scale adjacencies in a unified model.

While we presented the image in a graph structure, the model did not exploit any advanced graph properties other than the neighborhood structure. Applying graph processing techniques to our proposed representation should present an interesting topic to pursue in further work.

Phase retrieval is in particular an interesting and challenging problem, in which the HIO algorithm is still preferred for the case of non-sparse images. The phase retrieval algorithm presents several further challenges in terms of accurate noise estimation and efficiency. The noise model used so far was heuristic. Better results may be obtained by using more realistic modelling and estimation of the local phase noise. The efficiency of the phase estimation has not been optimized so far. That can be obtained by using advanced tree-based methods, suitable for the local phase structure as sub-trees of a wavelet decomposition tree.

ACKNOWLEDGEMENT

This research was supported in part by the Israeli Chief Scientist under the National Consortium OMEK, and by the Ollendorff Minerva Center.

APPENDIX A

EFFECTS OF GLOBAL PHASE DEVIATION ON LOCAL FREQUENCY COEFFICIENTS

To capture the essence of the relationship between global and local phase, we analyze 1D signals in a discrete domain, that can be further elaborated to deal with 2D signals. The Fourier transforms are discrete Fourier transforms, i.e. DFT, and the convolutions are also discrete. We use local analysis by means of the STFT for simplicity.

Let $x(t)$ denote a 1D signal of a discrete index t , and $\hat{x}(f)$ its Fourier transform. Let $x'(t)$ denote a signal identical to $x(t)$ other than a small perturbation η in the phase of one of the components:

$$\begin{aligned} \hat{x}'(f_0) &= \hat{x}(f_0) e^{j2\pi\eta} \\ x'(t) &= \mathcal{F}^{-1}\{\hat{x}'(f)\}(t). \end{aligned}$$

$x'(t)$ is then given by

$$\begin{aligned} x'(t) &= \sum_{f \neq f_0} \hat{x}'_f e^{j2\pi f \frac{t}{N}} + \sum_{f=f_0} \hat{x}'_f e^{j2\pi f \frac{t}{N}} \\ &= \tilde{x}(t) + \hat{x}_{f_0} e^{j2\pi f_0 \frac{t}{N}} e^{j\eta} \\ &= x(t) + \hat{x}_{f_0} e^{j2\pi f_0 \frac{t}{N}} (e^{j\eta} - 1) \\ &\approx x(t) + \hat{x}_{f_0} e^{j2\pi f_0 \frac{t}{N}} \cdot j\eta, \end{aligned}$$

where $\tilde{x}(t)$ is the signal $x(t)$ without the component in the frequency f_0 .

Next, we analyze the local frequency coefficients of $x'(t)$ via STFT:

$$\begin{aligned}\hat{x}'(t_0, f) &= \sum_t x'(t) w_{t-t_0} e^{-j2\pi f \frac{t}{N}} \\ &\approx \sum_t x(t) w_{t-t_0} e^{-j2\pi f \frac{t}{N}} + \\ &\quad + \sum_t \hat{x}_{f_0} e^{j2\pi f_0 \frac{t}{N}} j\eta \cdot w_{t-t_0} e^{-j2\pi f \frac{t}{N}} \\ &= \hat{x}(t_0, f) + \eta \cdot j\hat{x}_{f_0} \sum_t w_{t-t_0} \cdot e^{j2\pi(f_0-f)t/N} \\ &\triangleq \hat{x}(t_0, f) + \eta \cdot j\hat{x}_{f_0} \cdot z(f; t_0, f_0),\end{aligned}$$

where

$$\begin{aligned}z(f; t_0, f_0) &= \sum_t w_{t-t_0} \cdot e^{j2\pi(f_0-f)t/N} \\ &= e^{j2\pi(f_0-f)t_0/N} \cdot \sum_t w_{t-t_0} \cdot e^{j2\pi(f_0-f)\frac{t-t_0}{N}} \\ &\triangleq e^{j\beta} \cdot \sum_t w_{t-t_0} \cdot e^{j2\pi(f_0-f)(t-t_0)/N} \\ |z(f; t_0, f_0)| &= \left| \sum_t w_{t-t_0} \cdot e^{j2\pi(f_0-f)(t-t_0)/N} \right|.\end{aligned}$$

Let us consider the above absolute value, $|z(f; t_0, f_0)|$; it does not depend on t_0 due to the summation over t . It is a Fourier transform of a window function (sinc) shifted by frequency f_0 . It, therefore, decreases in absolute value in frequencies near f_0 .

Let us return to

$$\hat{x}'(t_0, f) \approx \hat{x}(t_0, f) + \eta \cdot \hat{x}_{f_0} \cdot e^{j\alpha} |z(f; t_0, f_0)|,$$

where $e^{j\alpha} = j e^{j\beta} = e^{j(\pi/2+\beta)}$ is some phase addition. We observe that the global phase shift of a frequency f_0 by a quantity η is expressed approximately in the local frequency domain via an addition that is scaled by the phase shift, η and the global frequency component \hat{x}_{f_0} . Further, it is localized in the local frequency f_0 which is the same as the global frequency, and its localization depends on the width of the windowing function w_{t-t_0} . It does not depend on the spatial location, t_0 .

This analysis shows that a shift (e.g. distortion) in global phase, expressed by the parameter η for some frequency f_0 , degrades the local coefficients with the same frequency f_0 by a linear addition (scaled by η) that affects both magnitude and phase of the local coefficient.

This relationship does not indicate that simply enforcing the correct local phase will necessarily have the effect of minimizing the distortion parameter η . We, therefore, resort to the following demonstration; let us now consider an edge signal $x(t)$:

$$x(t) = \begin{cases} 1, & t \geq 0 \\ -1, & t < 0. \end{cases}$$

It has zero global phase. Further, assume that we obtain $x'(t)$ by applying a phase deviation η and inspect the local

frequencies of $\hat{x}'(t_0, f)$ at $t_0 = 0$. Locally we observe the same edge structure with zero phase. In this case, we have:

$$\begin{aligned}\hat{x}'(t_0, f) &\approx |\hat{x}(t_0, f)| e^{j\angle\hat{x}(t_0, f)} + \eta \cdot |\hat{x}_{f_0}| \cdot \\ &\quad \cdot |z(f; t_0, f_0)| e^{j(\alpha+\angle\hat{x}_{f_0})} \\ &= |\hat{x}(t_0, f)| + \eta \cdot |\hat{x}_{f_0}| |z(f; t_0, f_0)| e^{j\alpha},\end{aligned}$$

where the only complex term is $e^{j\alpha} = j e^{j\beta}$, where β is a phase shift caused by the shifted spatial window function. We observe that in this case, enforcing the correct local phase will necessarily lead to $\eta = 0$, i.e. the correct global phase as well.

REFERENCES

- [1] I Zachevsky and Y Y Zeevi. Single-Image Superresolution of Natural Stochastic Textures Based on Fractional Brownian Motion. *IEEE Trans. Image Process.*, 23(5):2096–2108, 2014.
- [2] Ido Zachevsky and Yehoshua Y Zeevi. Statistics of Natural Stochastic Textures and Their Application in Image Denoising. *IEEE Trans. Image Process.*, 25(5):2130–2145, 2016.
- [3] J R Fienup. Phase retrieval algorithms: a comparison. *Appl. Opt.*, 21(15):2758–2769, 1982.
- [4] Moshe Porat and Yehoshua Y. Zeevi. Localized Texture Processing in Vision: Analysis and Synthesis in the Gaborian Space. *IEEE Trans. Biomed. Eng.*, 36(1):115–129, 1989.
- [5] Jacques Behar, Moshe Porat, and Yehoshua Y Zeevi. Image Reconstruction from Localized Phase. *IEEE Trans. Signal Process.*, 40(4):736–743, 1992.
- [6] Ivan W. Selesnick, Richard G. Baraniuk, and Nick G. Kingsbury. The dual-tree complex wavelet transform. *IEEE Signal Process. Mag.*, 22(6):123–151, 2005.
- [7] P. Kovsi. Image Features from Phase Congruency. *Videre*, 1(3):C3–C3, 1999.
- [8] D. Rotem and Y. Zeevi. Image reconstruction from zero crossings. *IEEE Trans. Acoust.*, 34(5), 1986.
- [9] P. Kovsi. Image Features from Phase Congruency. *Videre*, 1(3):C3–C3, 1999.
- [10] Rajiv Singh, Richa Srivastava, Om Prakash, and Ashish Khare. DTCWT based multimodal medical image fusion DTCWT Based Multimodal Medical Image Fusion. (January 2012):12–16, 2016.
- [11] Ryan Anderson, Nick Kingsbury, and Julien Fauqueur. Coarse-level object recognition using interlevel products of complex wavelets. *Proc. - Int. Conf. Image Process. ICIP*, 1:745–748, 2005.
- [12] Ryan Anderson, Nick Kingsbury, and Julien Fauqueur. Determining multiscale image feature angles from complex wavelet phases. *Lect. Notes Comput. Sci. (including Subser. Lect. Notes Artif. Intell. Lect. Notes Bioinformatics)*, 3656 LNCS(section 2):490–498, 2005.
- [13] Mark Miller and Nick Kingsbury. Image denoising using derotated complex wavelet coefficients. *IEEE Trans. Image Process.*, 17(9):1500–11, 2008.
- [14] Mark Miller and Nick Kingsbury. Statistical image modelling using interscale phase relationships of complex wavelet coefficients. In *IEEE Int. Conf. Acoust. Speech Signal Process.*, pages 789–792, 2006.
- [15] Zhou Wang and Ep Simoncelli. Local phase coherence and the perception of blur. *Adv. neural Inf. ...*, (December 2003):9–11, 2003.
- [16] An Vo and Soontorn Orantara. A study of relative phase in complex wavelet domain: Property, statistics and applications in texture image retrieval and segmentation. *Signal Process. Image Commun.*, 25(1):28–46, 2010.
- [17] Harpreet Singh, Shekhar Verma, and Gaganpreet Kaur Marwah. The New Approach for Medical Enhancement in Texture Classification and Feature Extraction of Lung MRI Images by using Gabor Filter with Wavelet Transform. *Indian J. Sci. Technol.*, 8(35), 2015.
- [18] Yi Xu, Xiaokang Yang, Li Song, Leonardo Traversoni, and Wei Lu. QWT (Quaternion wavelet transform): Retrospective and New Applications. *Geom. Algebr. Comput. Eng. Comput. Sci.*, pages 1–526, 2010.
- [19] Moshe Porat and Yehoshua Y. Zeevi. The Generalized Gabor Scheme of Image Representation in Biological and Machine Vision. *IEEE Trans. Pattern Anal. Mach. Intell.*, 10(4):452–468, 1988.
- [20] Trevor Hastie, Robert Tibshirani, and Jerome Friedman. *The Elements of Statistical Learning*, volume 1. 2009.

- [21] Yang Cao, Yupin Luo, and Shiyuan Yang. Image Denoising With Gaussian Mixture Model. *2008 Congr. Image Signal Process.*, pages 339–343, 2008.
- [22] Daniel Zoran and Yair Weiss. From learning models of natural image patches to whole image restoration. In *IEEE Int. Conf. Comput. Vis.*, pages 479–486, Barcelona, Spain, nov 2011.
- [23] Gabriel Peyré. Manifold models for signals and images. *Comput. Vis. Image Underst.*, 113(2):249–260, feb 2009.
- [24] Eliyahu Osherovich, Michael Zibulevsky, and Irad Yavneh. Approximate Fourier phase information in the phase retrieval problem: what it gives and how to use it. *J. Opt. Soc. Am. A. Opt. Image Sci. Vis.*, 28(10):2124–31, 2011.
- [25] Yoav Shechtman, Amir Beck, and Yonina C. Eldar. GESPAR: Efficient Phase Retrieval of Sparse Signals. *IEEE Trans. Signal Process.*, 62(4):928–938, 2014.
- [26] Tamir Bendory, Robert Beinert, and Yonina C Eldar. Fourier Phase Retrieval: Uniqueness and Algorithms. *Compress. Sens. its Appl.*, (646804):55–91, 2017.
- [27] Kishore Jaganathan, Yonina C. Eldar, and Babak Hassibi. Phase Retrieval: An Overview of Recent Developments. *arXiv Prepr. arXiv1510.07713*, (1):1–24, 2015.
- [28] Rohan Chandra, Ziyuan Zhong, Justin Hontz, Val Mcculloch, Christoph Studer, and Tom Goldstein. PhasePack: A Phase Retrieval Library. *arXiv Prepr. arXiv1711.10175*, 1711, 2017.